

Generalization of the Circular Dichroism from Metallic Arrays That Support Bloch-Like Surface Plasmon Polaritons

X. Guo^{✉,†}, C. Liu, and H.C. Ong^{*}

Department of Physics, The Chinese University of Hong Kong, Shatin, Hong Kong, People's Republic of China



(Received 14 August 2020; revised 6 January 2021; accepted 15 January 2021; published 19 February 2021)

The broken mirror symmetry in subwavelength photonic systems has manifested many interesting chiroptical effects, such as optical rotation and circular dichroism. When such systems are placed periodically in a lattice form, in addition to intrinsic chirality, extrinsic chirality also takes part, and the overall effect depends not only on the basis and lattice but also the excitation configuration. Here, we study planar chiral nanohole arrays in square lattice that support Bloch-like surface plasmon polaritons (SPPs) and clarify how the system geometry and the excitation contribute to circular dichroism. By using temporal coupled mode theory, the dissymmetry factor and the scattering matrix of the arrays are analytically formulated. Remarkably, we find the dissymmetry factor depends only on the coupling polarization angle and the in-coupling phase difference between the *p*- and *s*-polarizations. Furthermore, the upper limit of the dissymmetry factor at ± 2 can be reached simply by orienting the lattice of the arrays for properly exciting the Bloch-like SPPs and at the same time making the basis mimic two orthogonal and relatively displaced dipoles, demonstrating the interplay between extrinsic and intrinsic chirality. The models have been verified by numerical simulations and experiments, yielding dissymmetry factors of 1.82 and 1.55, respectively, from the proposed dual slot system.

DOI: 10.1103/PhysRevApplied.15.024048

I. INTRODUCTION

In chemistry, a molecule is called chiral when it is not superimposable with its mirror image [1]. One of the most interesting properties of chiral molecules is their interaction with light. For example, they exhibit different absorptions under the illumination of right (R) and left (L) circularly polarized (CP) light, exhibiting the well-known circular dichroism (CD) [1]. Because the CD arising from chiral molecules and their mirror images are opposite in sign, it has become a very popular technique in differentiating the handedness of enantiomers [2]. Recently, this idea has been employed in photonics where the geometry of subwavelength optical systems is designed to break the mirror symmetry [3–10]. Remarkably, the light-matter interactions arising from chiral photonic systems follow those of their molecular counterparts very well. Both optical rotation (OR), which tilts the linear polarization of light about its optical axis, and CD are observed in chiral photonic systems [11–20]. As a result, intensive efforts have been devoted to designing and implementing nanoscale chiral systems for optimizing the chiroptical effects [3,4,21–26].

However, rationally designing chiral systems is not a trivial task. In fact, most of the studies on chiral photonics involve complex system geometry that cannot be analytically simplified. This is because those systems are no longer considered as point dipoles and expansion to higher orders is necessary [27–29]. In addition, when multiple resonances prevail, the coupling between them increases the complexity of the physical picture even further [30,31]. Therefore, the size and shape of the system play a vital role in governing the light-matter interactions [15,28,32]. The situation becomes even more complicated when such systems are placed in a lattice form where, in addition to the basis, both the lattice and the excitation configuration should also be considered properly [33–36]. Currently, numerical electrodynamic simulations are usually performed to identify the core structures of the system and then fine tune them in a step-by-step manner [15,28,37–41]. Likewise, experiments mostly rely on a trial-and-error approach and are supplemented with simulations when necessary [14,42–45]. However, these two methods are very time consuming and sometimes work as a black box, which often does not reveal much of the underlying physics. It is always desirable if the physical mechanisms of chiral photonics can be generalized despite the diversity of system geometry and excitation.

In general, when resonances are involved, both CD and OR are the consequences of the in- and out-coupling of light to and from the resonator. How the resonance is

*hcong@phy.cuhk.edu.hk

[†]Present address: Physics Department, University of Michigan, Ann Arbor, MI 48108, USA.

excited and dissipated under different polarizations determines the light absorption and scattering as well as the phase difference between the outgoing polarizations. For example, ideal CD requires the resonator to be completely absorbing for one circular polarization but scattering for the other [3,4,26]. On the other hand, in analogy to a half-wave plate, light polarization gets flipped when one of the linear polarizations encounters a π phase shift upon the excitation of the resonator [46]. Therefore, if one can generalize the excitation and dissipation mechanism of different system geometries and excitation conditions, the chiroptical effects of some specific systems may be controlled at will.

Here, we attempt to accomplish such a task on planar chiral nanohole arrays where Bloch-like surface plasmon polaritons (SPPs) are supported. In particular, we combine temporal coupled mode theory (CMT), electrodynamic simulation, and polarization- and angle-resolved reflectivity spectroscopy together to formulate the dissymmetry factor and the scattering matrix of 2D L-shaped Au nanohole arrays. We find the complex in-coupling constants, which consist of the coupling polarization angle and phase shift, play a significant role in determining the resulting CD and they are found to be strongly dependent on the system geometry and excitation configuration. The dissymmetry factor can be maximized to ± 2 when the in-coupling polarization angle is $\pm 45^\circ$ and the difference between the *p*- and *s*-phase shifts is $\pm 90^\circ$. More importantly, such conditions can be accomplished by decoupling the L-shaped basis into two relatively displaced orthogonal slots and, at the same time, orientating the incident plane and the lattice properly to excite the SPPs. The optimization manifests the interplay between extrinsic and intrinsic chirality, which are carefully controlled through the rational design of the coupling constants.

II. EXPERIMENT

We fabricate 2D L-shaped nanohole arrays using a focused ion beam (FIB). First, 300-nm-thick Au films are deposited on glass substrates by radio frequency magnetron sputtering. Then, different array patterns with areas of approximately 0.01 mm^2 are milled on the Au films by FIB. The plane-view scanning electron microscopy (SEM) image of one of the samples is shown in the inset of Fig. 1(a), showing it has period $P = 550 \text{ nm}$, a long and a short arm with width = 125 nm and lengths = 400 and 250 nm, and hole depth = $60 \pm 20 \text{ nm}$. Since the Au film is optically thick, the sample has no transmission. Once the sample is ready, it is transferred to a homebuilt optical microscope where angle- and polarization-resolved reflectivity measurements can be performed [47]. The setup is shown in Fig. 1(a). Briefly, a broadband supercontinuum laser is collimated and then passed through a set of polarizers, wave plates, and lenses before being focused onto

the back focal plane (BFP) of a $100\times$ objective lens with numerical aperture = 0.9. By displacing the focused spot across the BFP of the objective lens using a motorized translation stage, the light exiting from the objective lens is collimated again and the incident polar angle θ onto the sample is given by $\sin \theta = d/f$, where d is the distance between the focused spot and the optical axis of the objective lens and f is the focal length of the objective lens [48]. In addition, the azimuthal angle ϕ can be varied by a motorized rotation sample stage. The light reflected from the sample is then collected by the same objective lens and passes through another set of analyzers and lenses before being detected by a spectrometer-based charge-coupled device detector. For CD measurement, we focus on the modes that support only specular reflection so that the dissymmetry factor g is given as [1]

$$g = 2 \left(\frac{A_{\text{RCP}} - A_{\text{LCP}}}{A_{\text{RCP}} + A_{\text{LCP}}} \right) = 2 \left(\frac{R_{\text{LCP}} - R_{\text{RCP}}}{2 - R_{\text{RCP}} - R_{\text{LCP}}} \right), \quad (1)$$

where $A_{\text{LCP/RCP}}$ and $R_{\text{LCP/RCP}}$ are the absorptions and reflectivities taken under LCP and RCP light.

III. RESULTS

The polarization- and angle-resolved reflectivity mappings of the L-shaped nanohole array are presented here. The measurement configuration is shown in Fig. 1(b). At

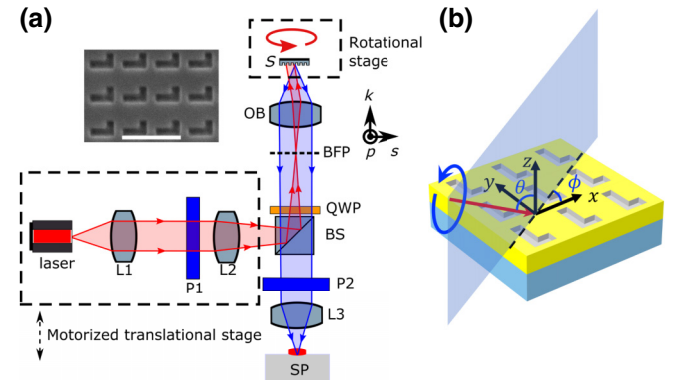


FIG. 1. (a) The setup for angle- and polarization-resolved optical microscopy where L , focusing lens; P , polarizer; BS , beam splitter; QWP , quarter-wave plate; BFP , back focal plane; OB , objective lens; S , sample; SP , spectrometer. The red beam indicates the incident beam path and the blue beam defines the scattered beam path from the sample. Inset: the plane-view SEM image of the FIB-fabricated L-shaped metallic nanohole array with the scale bar being $1 \mu\text{m}$. (b) The schematic of the sample and the excitation configuration. The blue region is the glass substrate while the yellow region is the gold thin film. The incident polar angle is defined as θ with respect to the surface normal, or the z direction, along the incident plane and the incident azimuthal angle is defined as ϕ between the incident plane and the Γ - X direction, i.e., the x direction.

$\theta = 45^\circ$, the ϕ -resolved reflectivity mappings taken under different polarizations, R_{pp} , R_{ps} , R_{sp} , and R_{ss} , are illustrated in Figs. 2(a)–2(d). The first and second subscripts of R indicate the collection and incident polarizations. We see from the R_{pp} and R_{ss} mappings that multiple low reflection dispersive bands are observed, and they can be identified by the SPP phase-matching equation given as [36]

$$\begin{aligned} \vec{k}_{\text{SPP}} &= \left(\frac{2\pi}{\lambda} \sin \theta \cos \varphi + \frac{n_x 2\pi}{P} \right) \hat{x} \\ &+ \left(\frac{2\pi}{\lambda} \sin \theta \sin \varphi + \frac{n_y 2\pi}{P} \right) \hat{y}, \end{aligned} \quad (2)$$

where \vec{k}_{SPP} is the propagation vector of the SPP mode defined with respect to the Γ - X direction and (n_x, n_y) are the indices specifying the Bragg scattering order. The propagation constant of SPPs $|\vec{k}_{\text{SPP}}| = \frac{2\pi}{\lambda} \sqrt{[(\varepsilon_{\text{Au}})/(1 + \varepsilon_{\text{Au}})]}$,

where ε_{Au} is the dielectric constant of gold [49]. Therefore, the reflection dips are the lowest order $(-1,0)$, $(0,-1)$ and $(1,0)$ SPPs in addition to the $(-1,-1)$ and $(1,-1)$ higher order modes at shorter wavelength. We find that the mappings are not symmetric with respect to $\phi = 90^\circ$ due to the presence of the chiral basis that breaks mirror symmetry. In particular, the reflectivity profiles from 35° to 90° and those from 90° to 145° are dramatically different. For example, at the 45° and 135° cross points where two propagating SPPs interact together to form a pair of bright and dark modes as well as a plasmonic band gap, one can see the gap is negligibly small at 45° but noticeable at 135° , indicating different coupling strengths [50].

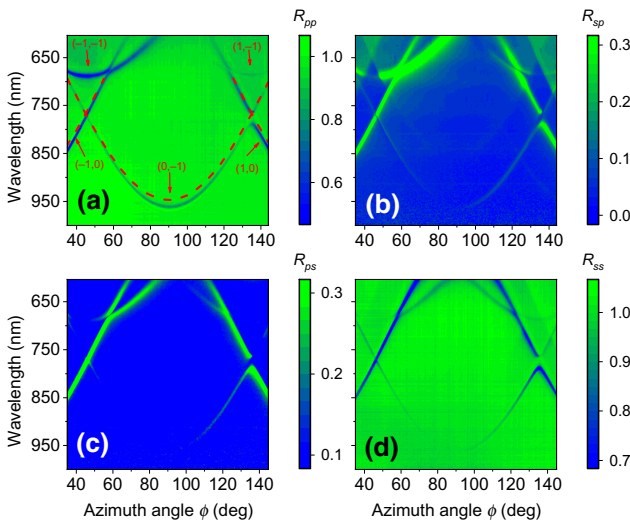


FIG. 2. The measured ϕ -dependent mappings of (a) R_{pp} , (b) R_{sp} , (c) R_{ps} and (d) R_{ss} . The SPP dispersion relations deduced from the analytical phase-matching equation are shown as red dashed lines in (a) and are labelled as (n_x, n_y) . The mappings are not symmetric with respect to $\phi = 90^\circ$ due to the chiral basis.

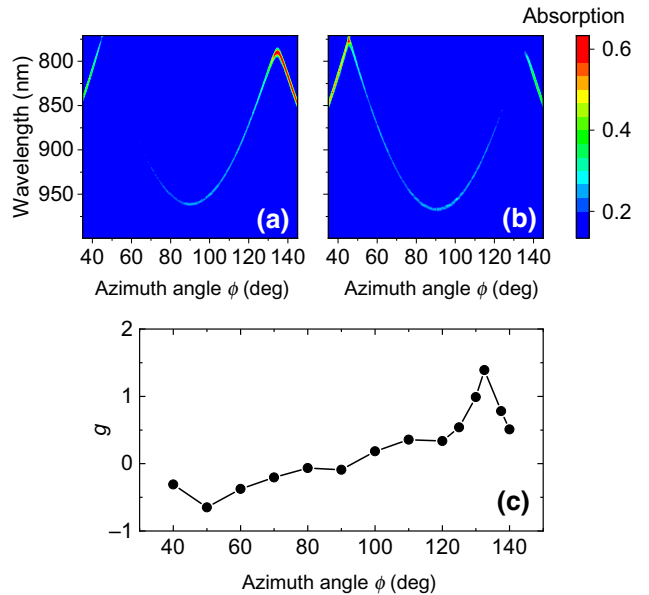


FIG. 3. The measured ϕ -dependent absorption mappings of the $(-1,0)$, $(0,-1)$, and $(1,0)$ SPP modes taken under (a) RCP and (b) LCP excitations. The color scale bars indicate the strength of absorption. (c) The plot of the dissymmetry factor g as a function of ϕ .

We also see strong polarization conversion in the R_{ps} and R_{sp} mappings, although their degrees of conversion are different, demonstrating the strong anisotropy introduced by the chiral basis. It is noted that both $(-1,0)$ and $(1,0)$ SPP modes exhibit stronger polarization conversion than the $(0,-1)$ mode.

We then measure the absorption mappings of the array taken under LCP and RCP light in Figs. 3(a) and 3(b) for $(-1,0)$, $(0,-1)$ and $(1,0)$ SPPs. These modes are chosen because they support only the specular reflection so that the dissymmetry factor g can be determined easily by Eq. (1). Again, the mappings are not symmetric with respect to $\phi = 90^\circ$. More importantly, the absorptions from the LCP and RCP light are different, indicating the presence of CD. We then calculate g along the lowest SPP bands as a function of ϕ , shown in Fig. 3(c). We observe g is almost zero when ϕ is close to 80° but exhibits a monotonic behavior before reaching the highest negative and positive g at the 45° and 135° cross points. In the following, we explain the behavior of g for the nondegenerate $(0,-1)$ SPPs excluding the cross points.

IV. FORMULATION OF DISSYMMETRY FACTOR

We attempt to formulate the g of the chiral plasmonic system within the framework of CMT [36,51–53]. We consider the system that supports one single resonance and two input-output ports for p - and s -polarizations. It therefore mimics an optically thick system that supports the lowest $(-1,0)$ SPPs where only specular reflection is present. The

dynamics of the mode amplitude a can be written as [51]:

$$\frac{da}{dt} = -i\omega_0 a - \frac{\Gamma_t}{2} a + \kappa_p s_{+p} + \kappa_s s_{+s}, \quad (3)$$

where ω_0 is the resonant angular frequency, Γ_t is the total decay rate, which is the summation of the absorption and radiative decay rates, i.e., $\Gamma_{\text{abs}} + \Gamma_{\text{rad}}$, κ_p and κ_s are the complex in-coupling constants for p - and s -polarizations, and s_{+p} and s_{+s} are the p - and s -polarized incident power amplitudes. It is noted that $\kappa_p = \sqrt{\Gamma_{\text{rad}}} \cos \alpha e^{i\delta_p}$ and $\kappa_s = \sqrt{\Gamma_{\text{rad}}} \sin \alpha e^{i\delta_s}$, where α is the coupling polarization angle and δ_p and δ_s are the in-coupling phase shifts [36,54]. Physically, α is the polarization angle, defined with respect to the p -polarization, where the excitation of SPPs is optimal [36,54]. In fact, Eq. (3) has been applied to 2D square lattice circular hole arrays in which α is related to the propagation direction of SPPs provided by Eq. (2). In addition, δ_p and δ_s are always equal due to the circular nanoholes [36].

Modification of Eq. (3) is necessary when extended to a chiral basis. For broken mirror symmetry, in analogy to planar birefringence, we expect α , and δ_p and δ_s to be amended. First, empirically, δ_p and δ_s are no longer identical, leading to different coupling phase shifts under the p - and s -polarizations [55–57]. Second, in addition to the lattice contribution, the anisotropy of the basis introduces an additional dipole contribution to α , giving rise to $\alpha = \alpha_{\text{lattice}} + \alpha_{\text{basis}}$, which is discussed later. When on resonance, where $\omega = \omega_0$, by solving Eq. (3), we have $|a|^2 = (2\Gamma_{\text{rad}}/\Gamma_t^2)[1 + \sin 2\alpha \cos(\delta_p - \delta_s - \gamma)]$, where γ is the phase difference between the p - and s -incident light.

Knowing from CMT that the absorption $A = \Gamma_{\text{abs}} |a|^2 / (|s_{+p}|^2 + |s_{+s}|^2)$ and the LCP and RCP light with $\gamma = \pm \pi/2$ are $\sqrt{\frac{1}{2}} \begin{bmatrix} 1 \\ i \end{bmatrix}$ and $\sqrt{\frac{1}{2}} \begin{bmatrix} 1 \\ -i \end{bmatrix}$, A_{RCP} and A_{LCP} can be expressed as $[(2\Gamma_{\text{rad}}\Gamma_{\text{abs}})/\Gamma_t^2][1 \mp \sin 2\alpha \sin(\delta_p - \delta_s)]$. Then, we reach our main result

$$g = -2 \sin 2\alpha \sin(\delta_p - \delta_s), \quad (4)$$

which arises primarily from the interference between two p - and s -excited SPPs. From Eq. (4), we see g varies between ± 2 and depends solely on α and $\delta_p - \delta_s$. In particular, if $\alpha = \pm 45^\circ$ and $\delta_p - \delta_s = \pm \pi/2$, g is highest. We explain this by examining the interference term $\mp \sin 2\alpha \sin(\delta_p - \delta_s)$, which depends on the amplitudes and the phase difference between the p - and s -excited SPP waves. For a given CP, when $\alpha = \pm 45^\circ$, both p - and s -waves are excited equally. At the same time, if $\delta_p - \delta_s = \pm \pi/2$, we see one CP will give constructive interference with $A = 4\Gamma_{\text{rad}}\Gamma_{\text{abs}}/\Gamma_t^2$ whereas the other yields destructive interference with $A = 0$. In other words, the system is absorbing for one CP but completely reflective for the other. Equation (4) also explains why circular nanohole

arrays do not give rise to any CD [36]. For a circular basis, despite $\alpha \neq 0^\circ$ under certain excitation configurations, $\delta_p - \delta_s$ is always equal to zero due to the lack of anisotropy. Finally, as both α and $\delta_p - \delta_s$ are system dependent, one can follow Eq. (4) to rationally design g .

It is noted that the picture described here is consistent with the recent work by Tang and Cohen [58,59]. In their work, the absorption taken under CP excitations is divided into two parts as $(\omega/2) \left(\alpha'' |\vec{E}|^2 + \chi'' |\vec{B}|^2 \right)$ and $G'' \omega \text{Im} (\vec{E}^* \cdot \vec{B})$, where \vec{E} and \vec{B} are the electric and magnetic fields and α'' , χ'' , and G'' are the imaginary part of the electric polarizability, the magnetic susceptibility, and the isotropic mixed electric-magnetic dipole polarizability. The first part is related to the electric and magnetic energy densities whereas the second is associated with optical chirality. CD thus arises from the difference between the energy density and the optical chirality from two CPs. For our case, although the Bloch-like SPP wave carries spin angular momentum (SAM), it only has transverse SAM that does not contribute to any optical chirality [60,61]. Therefore, the CD from our arrays is solely due to the difference in energy density, i.e., $|a|^2$, which agrees well with our CMT.

V. FORMULATION OF SCATTERING MATRIX

We then formulate the scattering matrix S of the system. We note that the L-shaped basis breaks not only the left-right mirror symmetry but also that of forward-backward under \vec{k} and $-\vec{k}$ incident light directions. The scattering matrix S , which is defined as $\begin{bmatrix} s_{-p} \\ s_{-s} \end{bmatrix} = S \begin{bmatrix} s_{+p} \\ s_{+s} \end{bmatrix}$, where s_{-p} and s_{-s} are the p - and s -polarized outgoing power amplitudes, is no longer symmetric but fulfills the following condition [62]:

$$S(\omega, \vec{k}) = S^T(\omega, -\vec{k}), \quad (5)$$

where the superscript T is the transpose of the matrix. Under forward \vec{k} incidence, s_{-p} and s_{-s} can be expressed as

$$\begin{bmatrix} s_{-p}^k \\ s_{-s}^k \end{bmatrix} = C \begin{bmatrix} s_{+p}^k \\ s_{+s}^k \end{bmatrix} + a^k \begin{bmatrix} d_p^k \\ d_s^k \end{bmatrix}, \quad (6)$$

where $C = \begin{bmatrix} \tilde{r}_{pp}^k & \tilde{r}_{ps}^k \\ \tilde{r}_{sp}^k & \tilde{r}_{ss}^k \end{bmatrix}$ is the complex direct reflection matrix and d_p and d_s are the complex out-coupling constants. For C , the first and second subscripts again denote the collection and incident polarizations. When we substitute a^k from Eqs. (3)–(6), we have

$$\begin{bmatrix} s_{-p}^k \\ s_{-s}^k \end{bmatrix} = \left[C + \frac{1}{i(\omega_o - \omega) + \Gamma_t/2} \begin{pmatrix} d_p^k \kappa_p^k & d_p^k \kappa_s^k \\ d_s^k \kappa_p^k & d_s^k \kappa_s^k \end{pmatrix} \right] \begin{bmatrix} s_{+p}^k \\ s_{+s}^k \end{bmatrix} = S(\omega, \vec{k}) \begin{bmatrix} s_{+p}^k \\ s_{+s}^k \end{bmatrix}, \quad (7)$$

which gives the scattering matrix $S(\omega, \vec{k})$. As is given in the Appendix, when combining Eqs. (5) and (7) together

$$\begin{aligned} S(\omega, \vec{k}) &= \begin{bmatrix} r_{pp}^k & r_{ps}^k \\ r_{sp}^k & r_{ss}^k \end{bmatrix} \\ &= \begin{bmatrix} \tilde{r}_{pp}^k + \frac{\Gamma_{\text{rad}} \cos \alpha_k^{\text{in}} \cos \alpha_k^{\text{out}} e^{i(\delta_p^k, \text{in} + \delta_p^k, \text{out})}}{i(\omega_o - \omega) + \Gamma_t/2} & \tilde{r}_{ps}^k + \frac{\Gamma_{\text{rad}} \sin \alpha_k^{\text{in}} \cos \alpha_k^{\text{out}} e^{i(\delta_s^k, \text{in} + \delta_p^k, \text{out})}}{i(\omega_o - \omega) + \Gamma_t/2} \\ \tilde{r}_{sp}^k + \frac{\Gamma_{\text{rad}} \cos \alpha_k^{\text{in}} \sin \alpha_k^{\text{out}} e^{i(\delta_p^k, \text{in} + \delta_s^k, \text{out})}}{i(\omega_o - \omega) + \Gamma_t/2} & \tilde{r}_{ss}^k + \frac{\Gamma_{\text{rad}} \sin \alpha_k^{\text{in}} \sin \alpha_k^{\text{out}} e^{i(\delta_s^k, \text{in} + \delta_s^k, \text{out})}}{i(\omega_o - \omega) + \Gamma_t/2} \end{bmatrix}, \end{aligned} \quad (8)$$

where the superscripts in and out define the in- and out-couplings, or the incident and reflection sides. We see, when under the \vec{k} direction, the reflection coefficients r in the matrix result from the interference between direct reflection and the radiation damping from SPPs. It is also noted that the incident and reflection polarization angles α and phase shifts δ_p and δ_s are different. The off-diagonal terms indicate polarization conversion. In particular, one can see complete polarization conversion occurs when the diagonal terms are zero but the off-diagonal terms are not. As $-\vec{k}$ is \vec{k} swiveled by 180° , for simplicity, we omit k in the expressions if not necessary.

VI. NUMERICAL SIMULATIONS

We validate the CMT models by electrodynamic simulations. We have performed finite element method (FEM) calculations using COMSOL and finite-difference time-domain calculations using software from Lumerical to simulate the complex reflection coefficient r , i.e., amplitude and phase, spectra of the $(0, -1)$ SPPs from an L-shaped Au array. The unit cell is shown in the inset of Fig. 4(a) and has period $P = 550$ nm, hole depth $H = 60$ nm, long and short arms $a = 400$ nm and $b = 250$ nm, and arm width $w = 125$ nm. The Bloch boundary condition is used on four sides. At a fixed polar incident angle $\theta = 45^\circ$, we use FEM to calculate the spectra as a function of ϕ under different incident and collection polarizations and two of them, taken at $\phi = 120^\circ$ and 300° , i.e., forward and backward incidences, are shown in Figs. 4(a)–4(h) and others are given in the Supplemental Material [63]. Comparing the complex r_{ps} and r_{sp} taken under two opposite incidences

with time-reversal symmetry and conservation of energy [51–53], we finally have

from Figs. 4(b), 4(c), 4(f) and 4(g), we see $r_{ps}^{k(-k)} \neq r_{sp}^{k(-k)}$, demonstrating $S(\omega, \vec{k})$ is not symmetric. In addition, it is also clear that $r_{pp}^k = r_{pp}^{-k}$, $r_{ss}^k = r_{ss}^{-k}$, and $r_{ps}^{k(-k)} = r_{sp}^{-k(k)}$, in agreement with Eqs. (5) and (8).

The amplitude and phase profiles are then best fitted by Eq. (8) to determine α^{in} and $\delta_p^{\text{in}} - \delta_s^{\text{in}}$ which are plotted in Figs. 5(a) and 5(b) against ϕ . Some examples are shown in Fig. 4 as solid lines, indicating reasonably good fits. Alternatively, we assume the incident wave has a functional form of $\begin{bmatrix} \cos \alpha \\ \sin \alpha e^{i\delta} \end{bmatrix}$, such that α and δ define the incident polarization angle and phase. We then systematically vary α and δ while at the same time monitoring the SPP near-field intensity. The α and δ that produce the strongest field intensity are also plotted in Figs. 5(a) and 5(b) and they agree with α^{in} and $\delta_p^{\text{in}} - \delta_s^{\text{in}}$ deduced from CMT. We thus interpret α^{in} and $\delta_p^{\text{in}} - \delta_s^{\text{in}}$ as the best incident polarization angle and phase difference that maximize the energy transfer from far-field to SPP near-field [36]. We note $\delta_p^{\text{in}} - \delta_s^{\text{in}}$ encounters discontinuity near $\phi = 80^\circ$. However, given $\alpha^{\text{in}} \approx 0^\circ$ where the best polarization is p -polarized and no s -polarized light can couple to the resonance, the in-coupling phase difference thus is ill-defined.

We also calculate g as a function of ϕ by using Eq. (4) and α^{in} and $\delta_p^{\text{in}} - \delta_s^{\text{in}}$, obtained from the field manipulation method, the best fits, as well as the direct FEM simulations taken under LCP and RCP light. Their results are plotted in Fig. 5(c), showing good agreement, with discrepancy of less than 10%. The experimental g from Fig. 3(c) is overlaid in Fig. 5(c), showing it is consistent with the simulations, that g is close to zero at $\phi \sim 80^\circ$ and exhibits

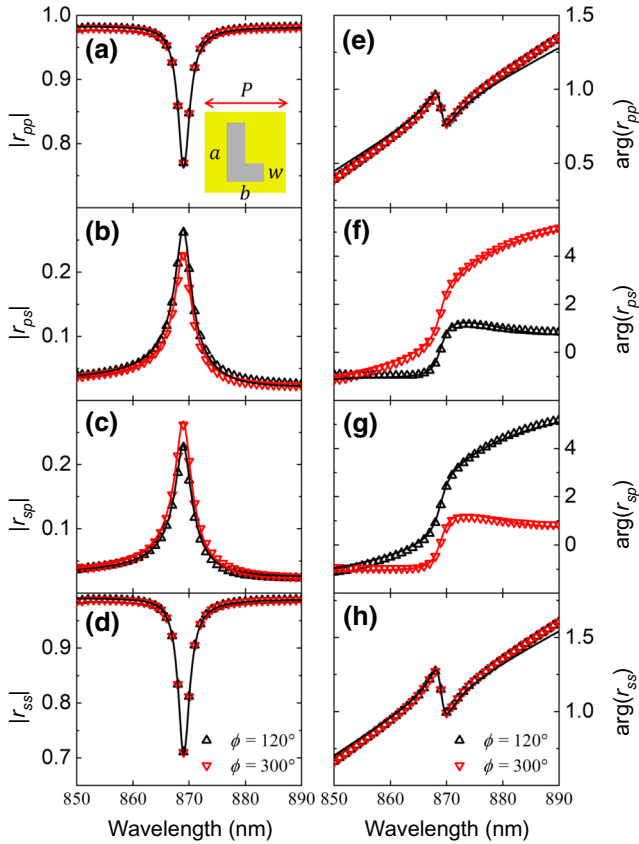


FIG. 4. The simulated (a)–(d) amplitudes and (e)–(h) phases of the reflection coefficients r_{pp} , r_{ps} , r_{sp} , and r_{ss} for $\phi = 120^\circ$ (forward incidence) and 300° (backward incidence). The solid lines are the best fits using the CMT deduced S . Inset: the schematic of the simulation unit cell with $P = 550$ nm, hole depth = 60 nm, $a = 400$, $b = 250$ nm, $w = 125$ nm.

similar monotonic behavior. Discrepancies are observed between experiment and simulation, particularly at small and large ϕ . However, discrepancies are always present due to the imperfection of the sample preparation, surface roughness, sample nonuniformity, etc., that are not easily removed completely. We also best fit the spectra extracted from Fig. 2 to determine α^{in} of the $(0, -1)$ SPPs as a function of ϕ in Fig. 5(a) and they are consistent with the simulation results. We therefore conclude both Eqs. (4) and (8) describe our system properly.

VII. DISCUSSION ON α

Before we move to rationally design the system to optimize g , it is essential to understand the physics behind α^{in} . For circular nanoholes, α^{in} is found to depend solely on the incident angle θ and the SPP propagation direction ρ and is given as [36]

$$\tan\alpha^{\text{in}} = \cos\theta \tan\rho, \quad (9)$$

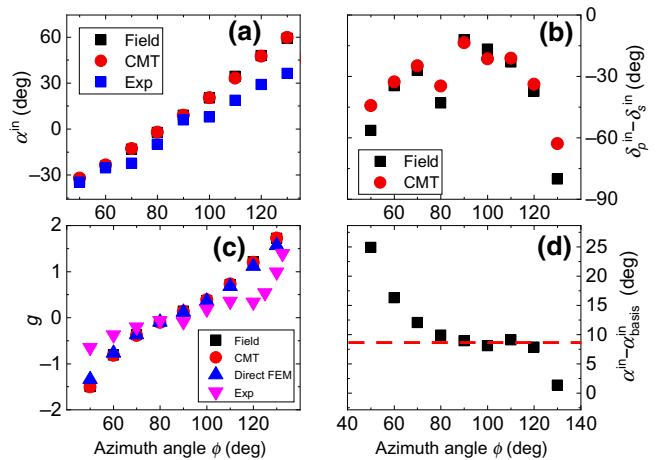


FIG. 5. (a) The α^{in} as a function of ϕ obtained by fitting the simulation and the experimental results with the CMT-deduced S and by using the field manipulation method. (b) The $\delta_p^{\text{in}} - \delta_s^{\text{in}}$ plot obtained by fitting the simulation with the CMT deduced S and by using the field manipulation method. (c) The g as a function of ϕ calculated by direct FEM and by using the α^{in} and $\delta_p^{\text{in}} - \delta_s^{\text{in}}$ given in (a) and (b) from CMT and field manipulation. The experimental results extracted from Fig. 3(c) are also overlaid for comparison. (d) The plot of $\alpha^{\text{in}} - \alpha_{\text{basis}}^{\text{in}}$ as a function of ϕ . It is almost constant with ϕ when away from the cross points.

where ρ is defined with respect to the incident plane based on Eq. (2). However, when anisotropy is introduced, α^{in} requires modification. We tackle this by comparing the α^{in} deduced from Eq. (9) and the calculations from Fig. 5(a) and observe a large discrepancy. The difference is taken and plotted in Fig. 5(d), showing the discrepancy is almost constant at 9° – 10° in the middle, in which the $(0, -1)$ SPP mode is nondegenerate but begins to increase and decrease to 25° and 1° when approaching the cross points at 45° and 135° . Such constant discrepancy implies the existence of an additional factor, which arises from the basis, that takes part in yielding the overall α^{in} . The same difference plot from another L-shaped nanohole array with the same basis but with $P = 800$ nm taken at $\theta = 5^\circ$ is provided in the Supplemental Material, supporting our observation [63]. Based on this, we propose α^{in} is contributed from both the lattice and basis as:

$$\alpha^{\text{in}} = \alpha_{\text{lattice}}^{\text{in}} + \alpha_{\text{basis}}^{\text{in}}, \quad (10)$$

Specifically, while $\alpha_{\text{lattice}}^{\text{in}}$ arises solely from the lattice following Eq. (9), $\alpha_{\text{basis}}^{\text{in}}$ strongly depends on the size, shape, and orientation of the basis. In particular, since Eq. (9) is formulated under the assumption that the best excitation occurs when the incident polarization aligns with the longitudinal electric field of SPPs, any deviation of α from $\alpha_{\text{lattice}}^{\text{in}}$ is most likely to come from the emergence of a field component that is orthogonal to the SPP propagation [35]. Unlike the circular basis, the anisotropy introduced by the

chiral L-shaped bases deviates the direction of the dipole moment and gives rise to an in-plane transverse field that effectively perturbs α .

To verify the idea, we have simulated two series of L-shaped arrays with different arm lengths and orientations. For the first series, four arrays with $P = 800$ nm and arm length being 125, 225, 425 and 625 nm as shown in Fig. 6(a) are simulated at $\theta = 5^\circ$ along the Γ - X direction. Their $\alpha_{\text{basis}}^{\text{in}}$ are plotted in Fig. 6(b). Provided $\rho = 0^\circ$, or $\alpha_{\text{lattice}}^{\text{in}} = 0^\circ$, we see when the basis is rectangular, i.e., arm length = 125 nm, in which the dipole moment is pointing along the Γ - X direction, it does not give rise to any $\alpha_{\text{basis}}^{\text{in}}$. However, as the arm length becomes longer and begins to swivel the dipole moment away from the Γ - X direction, $\alpha_{\text{basis}}^{\text{in}}$ increases correspondingly. We also calculate the electric field component perpendicular to the propagation direction of SPPs, i.e., the Γ - X direction, and find the strength increases consistently with increasing the arm length, as shown in Fig. 6(c). The second series further confirms the relationship between $\alpha_{\text{basis}}^{\text{in}}$ and the direction of the dipole moment. For the second series, we fix the geometry of the L-shape but vary its orientation. The basis is gradually rotated clockwise with respect to the Γ - X direction in Fig. 7(a) and the corresponding $\alpha_{\text{basis}}^{\text{in}}$ are determined in Fig. 7(b). We find $\alpha_{\text{basis}}^{\text{in}}$ changes monotonically as the L-shaped basis rotates, indicating the basis rotation simply swivels a fixed dipole moment gradually away from the Γ - X direction, thus increasing $\alpha_{\text{basis}}^{\text{in}}$. Again, the corresponding orthogonal electric field strength is plotted in Fig. 7(c) and it shows an identical pattern as that of $\alpha_{\text{basis}}^{\text{in}}$. As a result, we conclude an additional $\alpha_{\text{basis}}^{\text{in}}$ evolves when the basis becomes anisotropic. More importantly, we also see from Eq. (10) the subtlety of

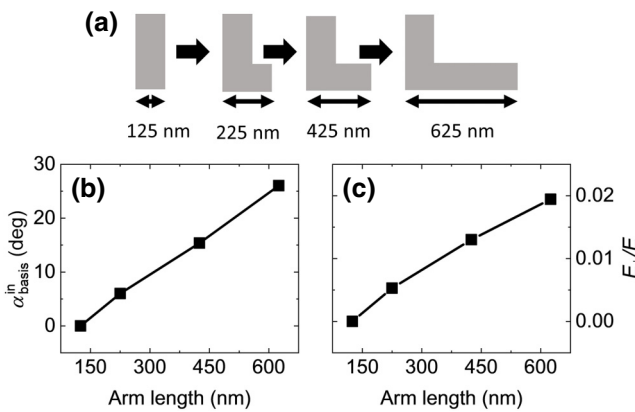


FIG. 6. (a) The evolution of the basis with arm length along the Γ - X direction. The arm length b is varied from 125 to 625 nm. (b) The variation of $\alpha_{\text{basis}}^{\text{in}}$ with b provided $\alpha_{\text{lattice}}^{\text{in}}$ is 0° all the time. (c) The plot of the ratio of the field amplitude perpendicular to the SPPs propagation direction E_{\perp} and the total field amplitude E as a function of b , showing a consistent behavior with $\alpha_{\text{basis}}^{\text{in}}$.

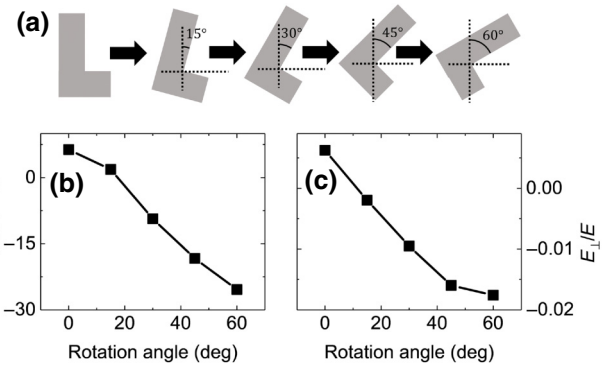


FIG. 7. (a) The evolution of the basis with orientation along the Γ - X direction. The rotation angle is varied from 0 to 60° with respect to the vertical axis. (b) The variation of $\alpha_{\text{basis}}^{\text{in}}$ with rotation angle provided $\alpha_{\text{lattice}}^{\text{in}}$ is 0° all the time. (c) The plot of the ratio of the field amplitude perpendicular to the SPPs propagation direction E_{\perp} and the total field amplitude E as a function of the rotation angle, showing a consistent trend.

$\alpha_{\text{basis}}^{\text{in}}$ arises from the interplay between intrinsic and extrinsic chirality. While $\alpha_{\text{lattice}}^{\text{in}}$ arises solely from the extrinsic chirality where only the relative orientation between the lattice and incident plane is relevant, $\alpha_{\text{basis}}^{\text{in}}$ is influenced by the strength of the dipole moment due to the symmetry breaking as well as its orientation with respect to the incident plane.

VIII. RATIONAL DESIGN OF DUAL SLOT SYSTEM

We are now in the position to rationally design the plasmonic arrays to achieve the best g by optimizing $\alpha_{\text{basis}}^{\text{in}}$ and $\delta_p^{\text{in}} - \delta_s^{\text{in}}$ close to $\pm 45^\circ$ and $\pm \pi/2$ following Eq. (4). We realize that when properly placed, the L-shaped nanohole can actually be pictured as two orthogonal slots with each excited independently by a linear polarization [64]. As a result, the nanohole can be decoupled into two separate slots, with each one exciting a dipole moment perpendicular to itself, as given in the Supplemental Material [63]. Therefore, the schematic of the basis is proposed in Fig. 8(a) with two perpendicular rectangular slots with the same slot width = 150 nm and depth = 100 nm, and lengths a and b separated by s . The whole basis is oriented by ψ to align with the incident plane.

The design process is divided into two steps for $\alpha_{\text{basis}}^{\text{in}}$ and $\delta_p^{\text{in}} - \delta_s^{\text{in}}$. First, we understand $\alpha_{\text{basis}}^{\text{in}}$ consists of $\alpha_{\text{lattice}}^{\text{in}}$ and $\alpha_{\text{basis}}^{\text{in}}$, which provide us a great degree of freedom for tuning $\alpha_{\text{basis}}^{\text{in}}$ to $\pm 45^\circ$. On one hand, $\alpha_{\text{lattice}}^{\text{in}}$ can be adjusted by following Eq. (9), orienting the lattice with respect to the incident plane. On the other hand, $\alpha_{\text{basis}}^{\text{in}}$ is governed by the lengths a and b as well as the orientation ψ . $\alpha_{\text{basis}}^{\text{in}}$ is also expected to be weakly dependent on s as the separation between two slots may affect the resulting dipole moment.

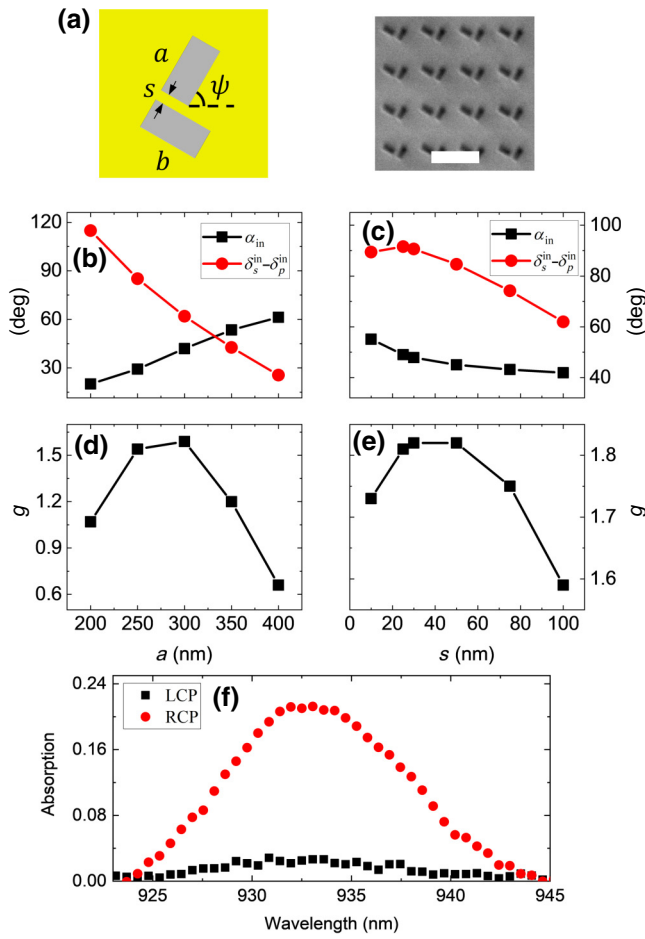


FIG. 8. (a) The unit cell of the proposed dual slot structure and the plane-view SEM image of the dual slot periodic structure fabricated by FIB with the scale bar = 1 μm . The plots of simulated (b) α_{in}^{in} and $\delta_p^{in} - \delta_s^{in}$ and (d) g as a function of a . The plots of simulated (c) α_{in}^{in} and $\delta_p^{in} - \delta_s^{in}$ and (e) g as a function of s . The highest g obtained from the two series are 1.52 and 1.82, respectively. (f) The absorption spectra of the (0,−1) SPP mode measured under LCP and RCP excitations, showing that g reaches 1.55.

As an illustration, we calculate α_{in}^{in} from a series of dual slot systems with $P = 800$ nm, $b = 300$ nm, $s = 100$ nm and $\psi = 60^\circ$, taken under $\theta = 10^\circ$ and $\phi = -120^\circ$ so that $\alpha_{lattice}^{in}$ is roughly close to 34° . The slots are positioned in parallel and perpendicular to the incident plane so that they can be independently excited by p - and s -polarizations. We then fine tune a from 200 to 400 nm in Fig. 8(b). It is found that α_{in}^{in} increases consistently with increasing a , verifying that α_{basis}^{in} is controlled by the relative strengths of the two orthogonal dipole moments with a larger dipole moment pointing in the direction perpendicular to the incident plane at large a . We also calculate α_{in}^{in} as a function of $s = 25$ to 100 nm from another series of dual slot systems in Fig. 8(c) with the same P , ψ , and b but the length a is fixed at 300 nm under the same excitation condition.

A weak dependence of α_{in}^{in} on s is observed. Noted from Figs. 8(b) and 8(c) that α_{in}^{in} is close to 45° when $a = 300$ nm and $s = 30$ nm.

Once the α_{in}^{in} is designed properly, we then move on to study the dependence of $\delta_p^{in} - \delta_s^{in}$ on the geometry. As $\delta_p^{in} - \delta_s^{in}$ is the phase difference arising from the p - and s -excited SPP waves, it can be controlled by spatially displacing two slots to introduce a dynamic phase difference between them. Therefore, varying a and s can be used for this introduction. We determine the $\delta_p^{in} - \delta_s^{in}$ from the previous two series of arrays in Figs. 8(b) and 8(c). The results show $\delta_p^{in} - \delta_s^{in}$ varies almost linearly with both a and s . $\delta_p^{in} - \delta_s^{in}$ is close to 90° at $a = 300$ nm and $s = 30$ nm. Based on the α_{in}^{in} and $\delta_p^{in} - \delta_s^{in}$, we calculate the corresponding g in Figs. 8(d) and 8(e) and find the highest g from the two series reach 1.5 and 1.82.

Following the simulation results, we fabricate a dual slot array by FIB as a demonstration. The plane-view SEM image of the system is shown in Fig. 8(a) and it shows the array has $P = 800$ nm, slot width = 150 nm, slot lengths a and $b = 300$ nm, and $s = 30$ nm. At $\theta = 10^\circ$ and $\phi = -120^\circ$, the absorption spectra are taken under RCP and LCP light and are plotted in Fig. 8(f). One sees the absorption peak observed at $\lambda = 933$ nm indicating the (0,−1) SPP mode and the absorption taken under RCP is much stronger than that under the LCP counterpart. The g is then deduced from the figure to be 1.55, which is slightly smaller than the expected 1.82. The discrepancy is very likely due to structural imperfection, especially the slot depth, which is very difficult to fabricate precisely by FIB. Finally, it is noted that the RCP absorption only reaches 0.21. To further boost the absorption, we see from $A_{RCP/LCP} = [(2\Gamma_{rad}\Gamma_{abs})/(\Gamma_t^2)][1 \mp \sin 2\alpha \sin(\delta_p - \delta_s)]$ that, other than α and $\delta_p - \delta_s$, A will reach unity in constructive interference when $\Gamma_{rad} = \Gamma_{abs}$, which is also known as critical coupling or complete absorption [65].

IX. CONCLUSION

In conclusion, we experimentally and theoretically study CD from 2D L-shaped nanohole arrays that support Bloch-like SPPs. Angle-resolved CD spectroscopy shows that CD has strong dependence on system geometry and orientation. CMT and numerical simulations are used to analytically formulate the dissymmetry factor g and the scattering matrix S of the arrays. In particular, g is found only to depend on two parameters, which are the best incident polarization angle α and the phase difference between p - and s -polarizations, $\delta_p - \delta_s$, that maximize the energy transfer from far-field to SPP near-field. While the former is further deconvoluted into the lattice and basis contributions, $\alpha_{lattice}^{in}$ and α_{basis}^{in} , the latter is determined by the phase

difference between the p - and s -excited SPPs. Nevertheless, they all manifest intrinsic and extrinsic chirality. On one hand, the basis acts like two rectangular slots in which their dimension and separation control the resulting dipole moment, which dominates α_{basis} and $\delta_p - \delta_s$. On the other hand, the relative orientation between the lattice and the incidence governs α_{lattice} . In order to maximize g , dual slot systems are then proposed. Guided by the CMT model, g as large as 1.82 and 1.55 can be obtained from simulation and experiment. Our results explain the CD effect mediated by single mode SPPs on periodic structures. The formalism can be readily generalized to different periodic structures which support SPPs since the effects of basis and lattice on CD are encoded into α and $\delta_p - \delta_s$. More importantly, it provides a systematic way of rationally designing the system for optimizing CD, which is much better than the conventional trial-and-error approach.

ACKNOWLEDGMENTS

This research was supported by the Chinese University of Hong Kong through Area of Excellence (AoE/P-02/12) and Innovative Technology Funds (ITS/133/19 and UIM/397).

APPENDIX: DERIVATION OF SCATTERING MATRIX

To solve for the elements in $S(\omega, \vec{k})$, we combine Eqs. (5) and (7) and find the following conditions:

$$\tilde{r}_{pp}^k = \tilde{r}_{pp}^{-k}, \quad (\text{A1})$$

$$\tilde{r}_{ss}^k = \tilde{r}_{ss}^{-k}, \quad (\text{A2})$$

$$\tilde{r}_{ps}^k = \tilde{r}_{sp}^{-k}, \quad (\text{A3})$$

$$\tilde{r}_{sp}^k = \tilde{r}_{ps}^{-k}, \quad (\text{A4})$$

$$d_p^k \kappa_p^k = d_p^{-k} \kappa_p^{-k}, \quad (\text{A5})$$

$$d_s^k \kappa_s^k = d_s^{-k} \kappa_s^{-k}, \quad (\text{A6})$$

$$d_p^k \kappa_s^k = d_s^{-k} \kappa_p^{-k}, \quad (\text{A7})$$

and

$$d_s^k \kappa_p^k = d_p^{-k} \kappa_s^{-k}. \quad (\text{A8})$$

It is expected that the off-diagonal elements are not the same, i.e., $\tilde{r}_{sp}^k \neq \tilde{r}_{ps}^k$ and $d_p^k \kappa_s^k \neq d_s^k \kappa_p^k$, because $S(\omega, \vec{k})$ itself is not symmetric. In addition, the in- and out-coupling constants are different, i.e., $d_p^k \neq \kappa_p^k$ and $d_s^k \neq \kappa_s^k$. To formulate the in- and out-coupling constants, we consider the time-reversal symmetry and assume the incidences are absent so that $(d|a^k|^2/dt) = -\Gamma_{\text{rad}}|a^k|^2 =$

$-(|s_{-p}^k|^2 + |s_{-s}^k|^2) = -(|d_p^k|^2 + |d_s^k|^2)|a^k|^2$ and $\Gamma_{\text{rad}} = |d_p^k|^2 + |d_s^k|^2$. We then can write $d_p^k = \sqrt{\Gamma_{\text{rad}}} \cos \alpha_k^{\text{out}} e^{i\delta_p^k}$ and $d_s^k = \sqrt{\Gamma_{\text{rad}}} \sin \alpha_k^{\text{out}} e^{i\delta_s^k}$, where α_k^{out} and $\delta_{p,s}^{k,\text{out}}$ are the out-coupling polarization angle and the p - and s -out-coupling phase shifts. Similarly, the in-coupling constants are $\kappa_p^k = \sqrt{\Gamma_{\text{rad}}} \cos \alpha_k^{\text{in}} e^{i\delta_p^k}$ and $\kappa_s^k = \sqrt{\Gamma_{\text{rad}}} \sin \alpha_k^{\text{in}} e^{i\delta_s^k}$. Once all the elements are available, we then compose $S(\omega, \vec{k})$ under the forward direction as in Eq. (8).

Note that combining Eqs. (A5) and (A7), together with Eqs. (A5) and (A8), we can get $\alpha_k^{\text{in}} = \alpha_{-k}^{\text{out}}$ and $\alpha_k^{\text{out}} = \alpha_{-k}^{\text{in}}$, respectively. As a result, the backward direction $S(\omega, -\vec{k})$ can be written in a similar fashion following the conditions provided in Eqs. (A1)–(A8) together with $\cos \alpha_k^{\text{in}} = \cos \alpha_{-k}^{\text{out}}$, $\cos \alpha_k^{\text{out}} = \cos \alpha_{-k}^{\text{in}}$, $\delta_p^{k,\text{in}} = \delta_p^{-k,\text{out}}$, and $\delta_p^{k,\text{out}} = \delta_p^{-k,\text{in}}$.

- [1] L. D. Barron, *Molecular Light Scattering and Optical Activity* (Cambridge University Press, Cambridge, 2004).
- [2] V. E. Bochenkov and T. I. Shabatina, Chiral plasmonic biosensors, *Biosensors* **8**, 120 (2018).
- [3] M. Schäferling, *Chiral Nanophotonics* (Springer, Cham, 2017).
- [4] M. Hentschel, M. Schäferling, X. Duan, H. Giessen, and N. Liu, Chiral plasmonics, *Sci. Adv.* **3**, 1602735 (2017).
- [5] M. J. Urban, C. Shen, X. Kong, C. Zhu, A. O. Govorov, Q. Wang, M. Hentschel, and N. Liu, Chiral plasmonic nanostructures enabled by bottom-up approaches, *Ann. Rev. Phys. Chem.* **70**, 275 (2019).
- [6] V. K. Valev, J. J. Baumberg, C. Sibilia, and T. Verbiest, Chirality and chiroptical effects in plasmonic nanostructures: Fundamentals, recent progress, and outlook, *Adv. Mater.* **25**, 2517 (2013).
- [7] Z. Hu, D. Meng, F. Lin, X. Zhu, Z. Fang, and X. Wu, Plasmonic circular dichroism of gold nanoparticle based nanostructures, *Adv. Opt. Mater.* **7**, 1801590 (2019).
- [8] J. T. Collins, C. Kuppe, D. C. Hooper, C. Sibilia, M. Centini, and V. K. Valev, Chirality and chiroptical effects in metal nanostructures: Fundamentals and current trends, *Adv. Opt. Mater.* **5**, 1700182 (2017).
- [9] Y. Luo, C. Chi, M. Jiang, R. Li, S. Zu, Y. Li, and Z. Fang, Plasmonic chiral nanostructures: Chiroptical effects and applications, *Adv. Opt. Mater.* **5**, 1700040 (2017).
- [10] H. Liu, D. A. Genov, D. M. Wu, Y. M. Liu, Z. W. Liu, C. Sun, S. N. Zhu, and X. Zhang, Magnetic plasmon hybridization and optical activity at optical frequencies in metallic nanostructures, *Phys. Rev. B* **76**, 073101 (2007).
- [11] A. Papakostas, A. Potts, D. M. Bagnall, S. L. Prosvirnin, H. J. Coles, and N. I. Zheludev, Optical Manifestations of Planar Chirality, *Phys. Rev. Lett.* **90**, 107404 (2003).
- [12] M. Kuwata-Gonokami, N. Saito, Y. Ino, M. Kauranen, K. Jefimovs, T. Vallius, J. Turunen, and Y. Svirko, Giant Optical Activity in Quasi-Two-Dimensional Planar Nanostructures, *Phys. Rev. Lett.* **95**, 227401 (2005).

- [13] J. Hao, Y. Yuan, L. Ran, T. Jiang, J. A. Kong, C. T. Chan, and L. Zhou, Manipulating Electromagnetic Wave Polarizations by Anisotropic Metamaterials, *Phys. Rev. Lett.* **99**, 063908 (2007).
- [14] F. Eftekhari and T. J. Davis, Strong chiral optical response from planar arrays of subwavelength metallic structures supporting surface plasmon resonances, *Phys. Rev. B* **86**, 075428 (2012).
- [15] H. Zhang and A. O. Govorov, Giant circular dichroism of a molecule in a region of strong plasmon resonances between two neighboring gold nanocrystals, *Phys. Rev. B* **87**, 075410 (2013).
- [16] T. Li, H. Liu, S. Wang, X. Yin, F. Wang, S. Zhu, and X. Zhang, Manipulating optical rotation in extraordinary transmission by hybrid plasmonic excitations, *Appl. Phys. Lett.* **93**, 021110 (2008).
- [17] A. Vázquez-Guardado and D. Chanda, Superchiral Light Generation on Degenerate Achiral Surfaces, *Phys. Rev. Lett.* **120**, 137601 (2018).
- [18] B. Bai, Y. Svirko, J. Turunen, and T. Vallius, Optical activity in planar chiral metamaterials: Theoretical study, *Phys. Rev. A* **76**, 023811 (2007).
- [19] S. Wu, Z. Zhang, Y. Zhang, K. Zhang, L. Zhou, X. Zhang, and Y. Zhu, Enhanced Rotation of the Polarization of a Light Beam Transmitted Through a Silver Film with an Array of Perforated S-Shaped Holes, *Phys. Rev. Lett.* **110**, 207401 (2013).
- [20] T. Q. Li, H. Liu, T. Li, S. M. Wang, F. M. Wang, R. X. Wu, P. Chen, S. N. Zhu, and X. Zhang, Magnetic resonance hybridization and optical activity of microwaves in a chiral metamaterial, *Appl. Phys. Lett.* **92**, 131111 (2008).
- [21] X. Wang, A. Díaz-Rubio, V. S. Asadchy, G. Ptitsyn, A. A. Generalov, J. Ala-Laurinaho, and S. A. Tretyakov, Extreme Asymmetry in Metasurfaces via Evanescent Fields Engineering: Angular-Asymmetric Absorption, *Phys. Rev. Lett.* **121**, 256802 (2018).
- [22] Y. Zhao, A. N. Askarpour, L. Sun, J. Shi, X. Li, and A. Alù, Chirality detection of enantiomers using twisted optical metamaterials, *Nat. Comm.* **8**, 14180 (2017).
- [23] T. Narushima, S. Hashiyada, and H. Okamoto, Nanoscopic study on developing optical activity with increasing chirality for two-dimensional metal nanostructures, *ACS Photonics* **1**, 732 (2014).
- [24] I. De Leon, M. J. Horton, S. A. Schulz, J. Upham, P. Banzer, and R. W. Boyd, Strong, spectrally-tunable chirality in diffractive metasurfaces, *Sci. Rep.* **5**, 13034 (2015).
- [25] M. H. Alizadeh and B. M. Reinhard, Plasmonically enhanced chiral optical fields and forces in achiral split ring resonators, *ACS Photonics* **2**, 361 (2015).
- [26] A. B. Khanikaev, N. Arju, Z. Fan, D. Purtseladze, F. Lu, J. Lee, P. Sarriugarte, M. Schnell, R. Hillenbrand, M. A. Belkin, and G. Shevts, Experimental demonstration of the microscopic origin of circular dichroism in two-dimensional metamaterials, *Nat. Comm.* **7**, 12045 (2016).
- [27] R. N. S. Suryadharma, C. Rockstuhl, O. J. F. Martin, and I. Fernandez-Corbaton, Quantifying Fano properties in self-assembled metamaterials, *Phys. Rev. B* **99**, 195416 (2019).
- [28] A. O. Govorov, Z. Fan, P. Hernandez, J. M. Slocik, and R. R. Naik, Theory of circular dichroism of nanomaterials comprising chiral molecules and nanocrystals: Plasmon enhancement, dipole interactions, and dielectric effects, *Nano. Lett.* **10**, 1374 (2010).
- [29] Z. Fan, H. Zhang, and A. O. Govorov, Optical properties of chiral plasmonic tetramers: Circular dichroism and multipole effects, *J. Phys. Chem. C* **117**, 14770 (2013).
- [30] N. Liu, H. Liu, S. Zhu, and H. Giessen, Stereometamaterials, *Nat. Photonics* **3**, 157 (2009).
- [31] H. Liu, J. X. Cao, S. N. Zhu, N. Liu, R. Ameling, and H. Giessen, Lagrange model for the chiral optical properties of stereometamaterials, *Phys. Rev. B* **81**, 241403 (R) (2010).
- [32] M. Schäferling, D. Dregely, M. Hentschel, and H. Giessen, Tailoring enhanced optical chirality: Design principles for chiral plasmonic nanostructures, *Phys. Rev. X* **2**, 031010 (2012).
- [33] E. Plum, V. Fedotov, and N. Zheludev, Optical activity in extrinsically chiral metamaterial, *Appl. Phys. Lett.* **93**, 191911 (2008).
- [34] S. S. Kruk, A. N. Poddubny, D. A. Powell, C. Helgert, M. Decker, T. Pertsch, D. N. Neshev, and Y. S. Kivshar, Polarization properties of optical metasurfaces of different symmetries, *Phys. Rev. B* **91**, 195401 (2015).
- [35] E. Plum, X. Liu, V. A. Fedotov, Y. Chen, D. P. Tsai, and N. I. Zheludev, Metamaterials: Optical Activity Without Chirality, *Phys. Rev. Lett.* **102**, 113902 (2009).
- [36] Z. L. Cao, L. Y. Yiu, Z. Q. Zhang, C. T. Chan, and H. C. Ong, Understanding the role of surface plasmon polaritons in two-dimensional achiral nanohole arrays for polarization conversion, *Phys. Rev. B* **95**, 155415 (2017).
- [37] Z. Liu, Y. Xu, C. Ji, S. Chen, X. Li, X. Zhang, Y. Yao, and J. Li, Fano-enhanced circular dichroism in deformable stereo metasurfaces, *Adv. Mater.* **32**, 1907077 (2020).
- [38] G. Klös, M. Miola, and D. S. Sutherland, Increased refractive index sensitivity by circular dichroism sensing through reduced substrate effect, *J. Phys. Chem. C* **123**, 7347 (2019).
- [39] Y. Wang, J. Qi, C. Pan, Q. Wu, J. Yao, Z. Chen, J. Chen, Y. Li, X. Yu, Q. Sun, and J. Xu, Giant circular dichroism of large-area extrinsic chiral metal nanocrescents, *Sci. Rep.* **8**, 3351 (2018).
- [40] A. V. Kondratov, M. V. Gorkunov, A. N. Darinskii, R. V. Gainutdinov, O. Y. Rogov, A. A. Ezhov, and V. V. Artemov, Extreme optical chirality of plasmonic nanohole arrays due to chiral fano resonance, *Phys. Rev. B* **93**, 195418 (2016).
- [41] M. Schäferling, X. Yin, N. Engheta, and H. Giessen, Helical plasmonic nanostructures as prototypical chiral near-field sources, *ACS Photonics* **1**, 530 (2014).
- [42] B. Bai, J. Laukkonen, A. Lehmuskero, and J. Turunen, Simultaneously enhanced transmission and artificial optical activity in gold film perforated with chiral hole array, *Phys. Rev. B* **81**, 115424 (2010).
- [43] Y. Chen, J. Gao, and X. Yang, Chiral metamaterials of plasmonic slanted nanoapertures with symmetry breaking, *Nano Lett.* **18**, 520 (2018).
- [44] Z. Wang, B. H. Teh, Y. Wang, G. Adamo, J. Teng, and H. Sun, Enhancing circular dichroism by super chiral hot spots from a chiral metasurface with apexes, *Appl. Phys. Lett.* **110**, 221108 (2017).
- [45] B. M. Maoz, A. Ben Moshe, D. Vestler, O. Bar-Elli, and G. Markovich, Chiroptical effects in planar achiral plasmonic oriented nanohole arrays, *Nano Lett.* **12**, 2357 (2012).

- [46] D. H. Goldstein, *Polarized Light* (CRC Press, New York, 2011).
- [47] Z. L. Cao and H. C. Ong, Momentum-dependent group velocity of surface plasmon polaritons in two-dimensional metallic nanohole array, *Opt. Exp.* **24**, 12489 (2016).
- [48] B. Huang, F. Yu, and R. N. Zare, Surface plasmon resonance imaging using a high numerical aperture microscope objective, *Anal. Chem.* **79**, 2979 (2007).
- [49] P. B. Johnson and R. W. Christy, Optical constants of the noble metals, *Phys. Rev.* **6**, 4370 (1972).
- [50] C. Ropers, D. J. Park, G. Stibenz, G. Steinmeyer, J. Kim, D. S. Kim, and C. Lienau, Femtosecond Light Transmission and Subradiant Damping in Plasmonic Crystals, *Phys. Rev. Lett.* **94**, 113901 (2005).
- [51] H. A. Haus, *Waves and Fields in Optoelectronics* (Prentice-Hall, New Jersey, Englewood Cliffs, 1984).
- [52] S. Fan, in *Optical Fiber Telecommunications V* (Academic Press, Burlington, 2008).
- [53] J. Yoon, K. H. Seol, S. H. Song, and R. Magnusson, Critical coupling in dissipative surface-plasmon resonators with multiple ports, *Opt. Exp.* **18**, 25702 (2010).
- [54] M. Lin, Z. L. Cao, and H. C. Ong, Determination of the excitation rate of quantum dots mediated by momentum-resolved Bloch-like surface plasmon polaritons, *Opt. Exp.* **25**, 6092 (2017).
- [55] B. T. Hallam, C. R. Lawrence, I. R. Hooper, and J. R. Sambles, Broad-band polarization conversion from a finite periodic structure in the microwave regime, *Appl. Phys. Lett.* **84**, 849 (2004).
- [56] D. C. Flanders, Submicrometer periodicity gratings as artificial anisotropic dielectrics, *Appl. Phys. Lett.* **42**, 492 (1983).
- [57] F. Xu, R. Tyan, P. Sun, Y. Fainman, C. Cheng, and A. Scherer, Fabrication, modeling, and characterization of form-birefringent nanostructures, *Opt. Lett.* **20**, 2457 (1995).
- [58] Y. Tang and A. E. Cohen, Optical Chirality and its Interaction with Matter, *Phys. Rev. Lett.* **104**, 163901 (2010).
- [59] Y. Tang and A. E. Cohen, Enhanced enantioselectivity in excitation of chiral molecules by superchiral light, *Science* **332**, 333 (2011).
- [60] K. Y. Bliokh, D. Smirnova, and F. Nori, Quantum spin Hall effect of light, *Science* **348**, 1448 (2015).
- [61] K. Y. Bliokh, A. Y. Bekshaev, and F. Nori, Extraordinary momentum and spin in evanescent waves, *Nat. Comm.* **5**, 3300 (2014).
- [62] N. A. Gippius, S. G. Tikhodeev, and T. Ishihara, Optical properties of photonic crystal slabs with an asymmetrical unit cell, *Phys. Rev. B* **72**, 045138 (2005).
- [63] See Supplemental Material <http://link.aps.org/supplemental/10.1103/PhysRevApplied.15.024048> for the FEM simulated complex reflection coefficient, r , spectra of the $(0,-1)$ SPPs from the L-shaped Au array taken at $\theta = 45^\circ$ and different ϕ , and the best fits by CMT; the simulated $(\alpha^{\text{in}} - \alpha_{\text{lattice}}^{\text{in}})$ by ϕ plot from the L-shaped nanohole array with $P = 800$ nm, $H = 60$ nm, $a = 400$ and $b = 250$ nm, and $w = 125$ nm, taken at $\theta = 5^\circ$; the electric near-field patterns of the dual slot excited by p - and s -polarized light.
- [64] J. Lin, J. P. Balthasar Mueller, Q. Wang, G. Yuan, N. Antoniou, X. C. Yuan, and F. Capasso, Polarization-controlled tunable directional coupling of surface plasmon polaritons, *Science* **340**, 331 (2013).
- [65] Z. L. Cao, L. Zhang, C. Y. Chan, and H. C. Ong, Interplay between absorption and radiative decay rates of surface plasmon polaritons for field enhancement in periodic arrays, *Opt. Lett.* **39**, 501 (2014).